Dalton Transactions

Synthesis and Electrochemical properties of metal(II)-carboxyethylphenylphosphinates

Journal:	*Dalton Transactions*
Manuscript ID	DT-ART-01-2021-000104.R1
Article Type:	Paper
Date Submitted by the Author:	18-Mar-2021

Complete List of Authors:	Bazaga García, Montse; Universidad de Malaga, Química Inorgánica, Cristalografía y Mineralogía Vílchez, Álvaro; Universidad de Malaga, Química Inorgánica, Cristalografía y Mineralogía Maranescu, Bianca; Institute of Chemistry Timisoara of Romanian Academy, Olivera Pastor, Pascual; Universidad de Malaga Facultad de Ciencias, Quimica Inorganica, Cristalografia y Mineralogia Marganovici, Marko; Institutul De Chimie Timisoara Al Academiei Romane Ilia, Gheorghe; Institutul De Chimie Timisoara Al Academiei Romane, Cabeza Díaz, Aurelio; Universidad de Málaga Facultad de Ciencias, Departamento de Quimica Inorganica, Cristalografia y Mineralogia Visa, Aurelia; Institute of Chemistry Timisoara of Romanian Academy Pérez Colodrero, Rosario; Universidad de Málaga Facultad de Ciencias, Dpto Química Inorgánica, Cristalografía y Mineralogía

ARTICLE

Synthesis and Electrochemical properties of metal(II)-carboxyethylphenylphosphinates

Montse Bazaga-García,[a] Álvaro Vílchez-Cózar,[a] Bianca Maranescu,[b] P. Olivera-Pastor[a], Marko Marganovici,[c] Gheorghe Ilia,[b,c] Aurelio Cabeza Díaz,[a] Aurelia Visa *[b] and Rosario M. P. Colodrero *[a]

Received 00th January 20xx,
Accepted 00th January 20xx

DOI: 10.1039/x0xx00000x

We report herein the synthesis, structural characterization and electrocatalytic properties of three new coordination polymers, resulting from the combination of divalent metal (Ca^{2+}, Cd^{2+} or Co^{2+}) salts with (2-carboxyethyl)(phenyl)phosphinic acid. In addition to the usual hydrothermal procedure, the Co^{2+} derivative could be also prepared by microwave-assisted synthesis, in much shorter times. The crystal structures were solved ab initio, from powder diffraction data. Compounds $M^{II}[O_2P(CH_2CH_2COOH)(C_6H_5)]_2$ {M= Cd (**1**) or Ca (**2**)} crystallize in the monoclinic system and display a layered topology, with the phenyl groups pointing toward the interlayer space in a interdigitated fashion. Compound $Co_2[(O_2P(CH_2CH_2COO)(C_6H_5)(H_2O)]_2{\cdot}2H_2O$ (**3**) presents a 1D structure composed of zig-zag chains, formed by edge-sharing cobalt octahedra, with phenyl groups pointing outside. Packing of these chains is favored by hydrogen bond interactions via lattice water. In addition, H-bonds along the chains are established with participation of the water molecules and the hydrophilic groups from the ligand. However, the solid exhibits a low proton conductivity, attributed to the isolation of the hydrophilic regions caused by the arrangement of hydrophobic phenyl groups. Preliminary studies on the electrocatalytical performance for the oxygen evolution reaction (OER) and oxygen reduction reaction (ORR) have been conducted for compound **3** and its pyrolytic derivatives, which were previously throughout characterized. By comparison, another Co^{2+} phosphinate, **4**, obtained by microwave-assisted synthesis, but with distinct stoichiometry and known structure was also tested. For OER, the best performance was reached with a derivative of **3**, prepared by heating this compound in N_2 at 200 °C. This derivative presented overpotential (339 mV, for a current density of 10 $mA{\cdot}cm^{-2}$) and Tafel slope (51.7 $mV{\cdot}dec^{-1}$) values comparable to other Co^{2+} related materials.

Introduction

To date, only few papers dealing with synthesis and properties of metal phosphinates have been published,[1] in contrast to the analogous multifunctional phosphonates-based coordination polymers, which have been profusely studied for several applications, among them proton conductors for Fuel Cells, electrodes for batteries and catalysts.[2] Available data on metal phosphinates indicate that the dimensionality of these solids is highly dependent on the type of the phosphinic acid (R_1R_2POOH) employed. So, monophosphinic acids usually lead to 1D solids, transition metal bisphosphinates form 2D networks,[3,4] whereas multifunctional ligands like those having both, carboxylic and phosphinic groups, e.g., (2-carboxyethyl)(phenyl)phosphinic acid, give rise to 2D or 3D networks.[5-9] By employing the latter ligand, Mn^{2+}- and Co^{2+}-derivatives, $M_3(L)_2(OH)_2$, with interesting magnetic properties were obtained.[5] Moreover, uranyl carboxyphosphinate derivatives, containing auxiliary N-donor ligands, showed promising physicochemical properties, including photoluminescence, photocatalytic properties, as well as relevant characteristics relative to the waste management and separation procedures of nuclear fuel.[10] Using the linker phenylene-1,4-bis(methylphosphinic acid), porous metal phosphinates have been recently reported and, more important, this porosity was shown to be dependent on the size of the organic groups.[11] Finally, by using auxiliary ligands,[12-14] a porous tubular 1D was synthesized from the reaction of a Cu(II) salt with the ligand 1,2-bis(4-pyridyl)ethane and P,P'-diphenyl-diphosphinate.[15]

On the other hand, phosphorus-containing coordination polymers have attracted attention as precursors, for obtaining versatile carbon-based materials, which are usable as electrocatalysts for fuel cells, electrolyzers or metal–air

[a] *Dpo Química Inorgánica, Cristalografía y Mineralogía, Facultad de Ciencias, Universidad de Málaga, Campus de Teatinos s/n, 29071-Málaga, Spain.*
[b] *"Coriolan Dragulescu" Institute of Chemistry, 24 Mihai Viteazu Bvd. 300223-Timisoara, Romania.*
[c] *West University Timisoara, Faculty of Chemistry, Biology, Geography, Dept. of Biology-Chemistry, 16 Pestalozzi Street, 300115, Timisoara, Romania.*

Electronic Supplementary Information (ESI) available: Fig. S1-S3: Rietveld plots for 1, 2, 3; Fig. S4: FT-IR spectra of 2, 3, 4; Fig. S5: Layered packing of 1; Fig. S6: Nyquist plots for CEPPA ligand and 3; Fig. S7: Arrhenius plots for CEPPA ligand and 3; Fig. S8: XRPD patterns for CEPPA ligand and 3 before and after proton conductivity measurements and for anhydrous and rehydrated compounds of 3; Fig. S9: XRPD patterns for pyrolyzed 3 derivatives; Fig. S10: XRPD patterns for pyrolyzed 4 derivatives; Fig. S11: Nyquist plots for selected derivatives; Fig. S12: LSV curves of selected pyrolyzed 3 and 4 derivatives for the ORR; Fig. S13: PXRD pattern of 3@1000C_N_2 after OER test; Fig. S14: XPS for Co $2p_{3/2}$ region of pyrolyzed derivative for 3, before and after OER and ORR tests; Table S1: Selected bond lengths (Å) for compounds 1 – 3; Table S2: H-bond distances for 3; Table S3: XS data for compound 3 and its pyrolyzed derivatives before and after OER and ORR tests. See DOI: 10.1039/x0xx00000x

batteries. These materials have been tested in key processes, such as the oxygen reduction reaction (ORR), oxygen evolution reaction (OER) and hydrogen evolution reaction (HER).[16-18] Furthermore, the electrocatalytic activity was found to be enhanced by heteroatom-doping of the carbon residues.[19,20] In line with this, ligands 1-Hydroxyethylidene-1,1-diphosphonic acid and pyrazine have been jointly employed to synthesize a copper derivative that, upon pyrolysis in N_2, transformed in Cu nanoparticles supported on N,P co-doped porous carbon.[21]

In this paper, we report the hydrothermal and/or microwave-assisted synthesis and their the structural characterization for three new carboxyethylphenylphosphinates of Ca, Cd and Co(II). In addition, we report, for the first time, preliminary results on the electrocatalytic behavior of two Co (II) phosphinate derivatives, one of them already structurally described in literature, for OER and ORR.

Experimental

Materials

Dichloro(phenyl)phosphine, acrylic acid, cobalt acetate tetrahydrate, calcium acetate monohydrate, cooper acetate monohydrate, cadmium acetate dihydrate and magnesium chloride were purchased from Sigma-Aldrich. All reagents were used without further purification.

Synthesis

Preparation of 2-Carboxyethylphenylphosphinic acid (CEPPA). The acid was prepared from dichloro(phenyl)phosphine and acrylic acid, according to literature.[22]

Preparation of $Cd[O_2P(CH_2CH_2COOH)(C_6H_5)]_2$ (1). A mixture of 2.2 mmol $Cd(CH_3COO)_2{\cdot}2H_2O$, 1.0 mmol $MgCl_2$, 4 mmol (2-Carboxyethyl)(phenyl)phosphinic acid, 8 mmol NaF, 70 mmol CH_3COOH and 16 ml of distilled water (DI) was heated at 120 °C for 36 h in a Teflon autoclave. After cooling at room temperature, the solid was isolated by filtration, washed several times with DI and dried at room temperature. Elemental composition (wt%): Anal. calcd for $CdC_{18}H_{20}O_8P_2$: C 40.13, H 3.74; found C 38.02, H 3.70.

Preparation of $Ca[O_2P(CH_2CH_2COOH)(C_6H_5)]_2$ (2) and $[Co_2(O_2P(CH_2CH_2COO)(C_6H_5))_2(H_2O)_2]{\cdot}2H_2O$ (3). 3 mmol $Ca(CH_3COO)_2{\cdot}H_2O$ or $Co(CH_3COO)_2{\cdot}4H_2O$ were dissolved in 10 ml distilled water and 3 mmol (2-carboxyethyl)(phenyl)phosphinic acid were dissolved also in 10 ml distilled water under moderate heating (60 °C). The solutions were mixed and kept under stirring for 1 hour at 50-60 °C then transferred in a stainless steel autoclave with a teflon autoclave (ca. 30 ml capacity) and kept at 130 °C for 24 hours. The obtained solids were filtered, washed with DI several times and air-dried at room temperature. Elemental composition (wt%): Anal. calcd for $CaC_{18}H_{20}O_8P_2$: C 46.36, H 4.32; found C 45.96, H 4.21. Anal. calcd for $Co_2C_{18}H_{26}O_{12}P_2$: C 35.20, H 4.27; found C 35.28, H 4.34.

Alternatively, compound **3** was also prepared by microwave assisted synthesis (Anton Paar Monowave 300 microwave) by reaction of the mixture in a 30 mL glass vial at 150 °C for 5 minutes and under constant magnetic stirring (600 rpm). The solid was recovered by centrifugation, washed with DI water and dried at room temperature. Longer reaction times (1h) led to the reported compound, $Co_3[O_2P(CH_2CH_2COO)(C_6H_5)]_2(OH)_2$ (**4**).[5]

Chemical and Physical Characterization. Elemental analyses (C, N and H) were performed with a Perkin-Elmer 240 analyzer. TG-DTA analysis were recorded on an SDT-Q600 (TA instruments). The temperature varied from RT to 1000 °C with a heating rate of 10 °C·min^{-1}. Measurements were carried out on samples in open platinum crucibles under a flow of air or N_2. Infrared spectra were recorded in the 4000 - 500 cm^{-1} range at 4 cm^{-1} resolution (64 scans accumulated) using an ATR accessory (Golden Gate Single Reflection Diamond ATR System) coupled to FTIR spectrometer (Vertexde Bruker).

X-ray diffraction characterization. The crystal structure of these compounds were determined from synchrotron X-ray powder diffraction data (SXRPD) or laboratory X-ray powder diffraction data (LXRPD). For **3**, SXRPD were collected at the high resolution BL04-MSPD beamline of ALBA, the Spanish Synchrotron Radiation Facility (Barcelona, Spain). A wavelength of 0.4124 Å was selected with a double-crystal Si (111) monochromator and determined from a Si640d NIST standard (a = 5.43123 Å) measurements, using a MYTHEM detector. The capillary was rotated during data collection to improve diffracting particle statistics and patterns were collected over the angular range 1.70 – 20° (2θ) or the d-space of 1.19-13.82Å. For the other compounds, **1** and **2**, LXRPD were collected on a D8 ADVANCE (Bruker AXS) diffractometer equipped with a Johansson Ge(111) primary monochromator giving a monochromatic Mo radiation (λ = 0.7093 Å) and using the energy-dispersive linear detector LYNXEYE XE 500 µm. Data were collected in the angular region 4.40 – 50° (2θ)) or the d-space of 0.84-9.21Å, with a step size of 0.01° and a counting time of ~1600 s/step.

For samples **2** and **3**, their crystal structures were solved by direct methods using the program EXPO2014.[23] The starting framework models, containing all atoms in the asymmetric part of the unit cell except those corresponding to water in case of **3**, were derived from interpretation of the electron density map computed with the set of refined phases with the highest combined figure of merit. For cadmium derivative, **1**, its crystal structure was obtained by simulated annealing procedure implement in EXPO2014[23] and using the structure of the orthorhombic polymorph[24] as starting model. The initial structural models were refined by the Rietveld method,[25] using the GSAS package[26] and the EXPGUI graphic interface.[27] The following soft constraints were imposed in order to preserve chemically reasonable geometries for the phosphinate, alkyl chain, and aromatic ring: /PO_2C_2 tetrahedron/P–O [1.53(1) Å], P–C [1.80(1) Å], O–O [2.55(2) Å], O–C [2.73(2) Å]; C1–C2[2.90(2) Å]; /C1–C2–C3OO group/C–C [1.50(1) Å], C1···C3 [2.50(2) Å], C3-O_{carb} [1.23(1) Å], $O_{carb}\cdots O_{carb}$ [2.21(2)Å] and C2···O_{carb} [2.36(2) Å] and /aromatic ring/ C–C [1.40(1) Å], $C_{ring}\cdots C_{ring}$ [2.40(1) Å], $C_{ring}\cdots C_{ring}$ [2.80(1) Å]. No attempts to locate the H atoms were carried out due to the limited quality of the XRPD data. For **1** and **3**, the final weight factor for the soft constraints was 10 and

three isotropic atomic displacement parameters were refined, one for the metal atom, a second for the P atoms and a third one for the rest of the atoms. For **2**, the final weight factor for the soft constrains was 15 and only two isotropic atomic displacement parameters were refined, one for the heavier atoms (Ca and P) and a second one for the rest of the atoms. Selected structural data are reported in Table 1 and the final Rietveld plot is given in the Supporting Information (SI) as Figures S1-S3.

Thermodiffractometric data were obtained in an Anton Paar HTK1200N Camera, under static air, on a PANanalytical X'Pert Pro automated diffractometer. Data were collected in Bragg-Brentano reflection configuration, with Cu $K_{\alpha 1}$ and the X'Celerator detector. Data were collected at different temperature intervals from room temperature up to 180 °C for **3**. A heating rate of 5 °C·min^{-1} and a delay time of 5 minutes to ensure thermal stabilization were used. PXRD patterns were recorded in the region 4 - 70° (2θ), with a step size of 0.017° - 0.033° and an equivalent counting time of ~57 – 100 s/step.

Table 1 Crystallographic Data and Structure Refinements for M-CEPPA derivatives

	1	**2**	**3**
Space Group	$P2_1/n$	Pn	$P2_1/a$
Chemical formula	$C_{18}H_{20}O_8P_2Cd$	$C_{18}H_{20}O_8P_2Ca$	$C_{36}H_{52}O_{24}P_4Co_4$
Formula mass (g·mol^{-1})	538.71	466.37	1228.41
λ (Å)	0.7093	0.7093	0.4124
a (Å)	14.9484(4)	14.4949(7)	9.3919(2)
b (Å)	5.5197(1)	5.7690(3)	23.4056(6)
c (Å)	23.7152(5)	12.9059(5)	10.5199(3)
α (°)	90.0	90.0	90.0
β (°)	95.411(2)	113.432(2)	95.563(2)
γ (°)	90.0	90.0	90.0
V (Å^3)	1948.0(1)	990.2(1)	2301.6(1)
Z	4	2	2
Temperature (K)	298	298	298
d-space (Å)	9.02	9.21	13.82
Independent reflections	1830	1751	1441
Data/restrains/ parameters	3599/52/134	4630/73/138	3128/81/133
R_{WP}	0.0738	0.1042	0.1066
R_P	0.0553	0.0780	0.0794
R_F	0.0344	0.0457	0.0880
CCDC number	1993189	1993191	1993190

XPS characterization. The surface composition and chemical environment were carried out by X-ray photoelectron spectroscopy. Analyses were performed on a Physical Electronics ESCA 5701 spectrometer.

Proton Conductivity Studies. Impedance measurements of the powdered polycrystalline compounds were carried out on cylindrical pellets (~5 mm diameter; ~1.22–0.73 mm thickness) obtained by pressing ~30-40 mg of sample at 250 MPa for 1 min between porous C electrodes (Sigracet, GDL 10 BB, no Pt). Pellets were placed inside a temperature and humidity controlled chamber (Espec SH-222). Impedance data were collected using an AUTOLAB PGSTAT302N impedance analyzer equipped with a Frequency Response Analyzer (FRA) module over the frequency range from 20 Hz to 1 MHz with an applied voltage of 0.35V. All measurements were electronically controlled by the Nova package of programs. In order to equilibrate the water content, pellets were first preheated (0.2 °C/min) from 25 to 80 °C at 95 %RH. Impedance spectra were recorded on cooling using stabilization times of 5 h for each temperature (80, 70, 60, 50, 40, 30 and 25 °C). Water condensation on the sample was avoided by reducing first the relative humidity before decreasing temperature. The total pellet resistance (R_T) was obtained by fitting to the equivalent circuit models from the Nyquist plots at different temperatures.

Electrochemical measurements. Electrochemical measurements for compounds **3** and **4** were carried out with a BioLogic VSP-128 potentiostat/galvanostat having a built-in electrochemical impedance spectroscopy analyzer. The electrochemical activity of the catalysts was measured in a typical three-electrode configuration using a 5 mm diameter glassy carbon rotating disc electrode (RDE, area= 0.196 cm^2, Methrom Autolab) as working electrode and the platinum rod and Ag/AgCl (3M KCl) electrode used as the counter and reference electrodes, respectively. For the preparation of the working electrode, 4 mg of catalysts and 1.3 mg of carbon black (Super P® Conductive, <99%, Alfa Aesar) were dispersed into 470 µL of ethanol/H_2O (v/v = 1/1, Milli-Q Water, 18 MΩ·cm^{-1} and ethanol, >99.5%, Sigma Aldrich) with 30 µL of 5 wt% Nafion® solution (Nafion® 117 solution, Sigma Aldrich) followed by sonication for 30 min to obtain a homogeneous ink. Then, 8.2 µL of the catalyst ink was spread out on the glassy carbon electrode by drop-coating and dried at room temperature to achieve a catalyst loading of 0.33 mg·cm^{-2}. For comparison, commercial 20 wt% Pt/C (HISPEC 3000, Johnson Matthey Company) was deposited on the glassy carbon with the same loading. Prior to catalyst deposition, the GC electrode was polished with 0.3 µm alumina slurry and then rinsed with deionized water and ethanol, sonicated for 3 min, and dried in air. All the current densities were normalized to the geometrical surface area of the electrodes, and the measured potential (versus Ag/AgCl) was converted to the potential (versus reversible hydrogen electrode, RHE) according to the Nernst equation [E(RHE) = E(Ag/AgCl) + 0.205 + 0.059pH]. All the electrochemical measurements were conducted with iR compensation.

The OER tests were performed in 1M KOH (KOH pure pellets, Sigma Aldrich) electrolyte at 25 °C with the RDE rotate at 1600

rpm. Cyclic voltammograms (CVs) and linear sweep voltammograms (LSVs) were measured at a scan rate of 20 and 10 mV·s^{-1} respectively in the potential window 1.0 to 1.7 V vs RHE. The overpotential was determined from the equation of η = E(RHE) – 1.23. The Tafel slope was calculated according to the Tafel equation: $\eta = a + b \log J$ where η, b, and J correspond to the overpotential, Tafel slope and the current density, respectively. Electrochemical impedance spectroscopy (EIS) measurements were carried out from 100 kHz to 0.1 Hz with an amplitude of 5 mV at 1.58 V vs RHE. Likewise, the ORR tests were conducted in 0.1M KOH electrolyte at 25 °C with the RDE rotate at 1600 rpm. Cyclic voltammograms (CVs) and linear sweep voltammograms (LSVs) were measured at a scan rate of 20 and 10 mV·s^{-1} respectively in the potential window 0.2 to 1.2 V vs RHE. The catalyst supported on carbon paper (1x1 cm^2) with 1 mg cm^{-2} loading was used to perform stability tests. Prior to the OER and ORR tests, the KOH electrolyte was bubbled for 30 min with N_2 and O_2 respectively and maintained over the whole measurement to ensure the gas saturation in the electrolyte.

The turnover frequency number (TOF) was obtained from the expression: $TOF = i/4Q$, where i is the current intensity and Q is the faradaic charge under the baseline-corrected voltametric peak preceding the electrocatalytic wave, and assuming a faradaic efficiency of 100 %.[28]

Results and discussion

Although the general method of synthesis for these compounds is a hydrothermal reaction for 24 h, crystalline Co(II) derivatives were also prepared by fast microwave-assisted synthesis within 60 min. The cadmium derivative here reported is a new polymorph of another one described elsewhere.[24] This polymorph, that crystallizes in the orthorhombic system (space group $Pca2_1$), was obtained by hydrothermal reaction at 120 °C, instead of 150 °C, and in the presence of a (0.0625 M) $MgCl_2$ solution, used to test the possibility of formation of solid solution derivatives. Although present in the solid, as revealed by SEM-EDX analysis, the Mg^{2+} ion does not incorporate to the crystal structure, but it is part of an accompanying amorphous impurity, which is responsible for a decrease in carbon percentage, relative to the pure crystalline solid.

On other hand, the IR spectra of compounds **1** and **2** (Figure S4) show a band at 1683 cm^{-1}, which is absent in spectra of **3** and **4**, indicative of the presence of a carboxylic group. For solid **3**, broad bands in the region of 3495 - 3322 cm^{-1}, together with the deformation vibration of H-O-H at 1638 cm^{-1}, indicate the presence of H-bonded water, in agreement with crystallographic data (see below). Other bands characteristic of phosphinate groups are also observed in the IR spectra.[24]

Crystal structure of $M^{II}[O_2P(CH_2CH_2COOH)(C_6H_5)]_2$, M^{II}= Cd (1) and Ca (2).

Compounds **1** and **2** crystallizes in the monoclinic system, space groups $P2_1/n$ and Pn, respectively, with similar a and b unit cell parameters, which define the organic-inorganic layers. Packing of the layers takes place along c axis direction, but in **1,** the c parameter is twofold (Table 1). Their crystal structures, solved *ab initio* from laboratory powder diffraction data, contain 29 non-hydrogen atoms in the asymmetric part of the unit cell, one M^{2+} ion and two $(Ph\text{-}PO_2\text{-}C_2H_4\text{-}COOH)^-$ ligands crystallographically independent (Figure 1). Both compounds exhibit similar structural characteristics with divalent cation in a distorted octahedral environment (Table S1) surrounded by four phosphinate oxygen atoms and two carboxylate oxygen atoms from six ligands. The layers are composed of chains of isolated MO_6 polyhedra interconnected by bridging phosphinate groups, into a near-planar 8-membered ring (A), along the b direction (Figure 1) with intra-chain $M^{2+}\cdots M^{2+}$ distances (d_1) of 5.52 Å (Cd^{2+}) and 5.77 Å (Ca^{2+}). Neighbouring chains are interconnected by monodentate alkyl carboxylic groups, along the *a-axis* direction, forming 14-membered rings (B) between two metal centres and two ligands. In the a direction, the $M^{2+}\cdots M^{2+}$ distance is kept at ~7.60 Å (d_2), while in the cadmium derivative two different slightly distances are found, at 7.57 and 7.60 Å. This M^{2+}-ligand connectivity mode has been also reported for other cadmium phosphinates, including the orthorhombic polymorph.[24]

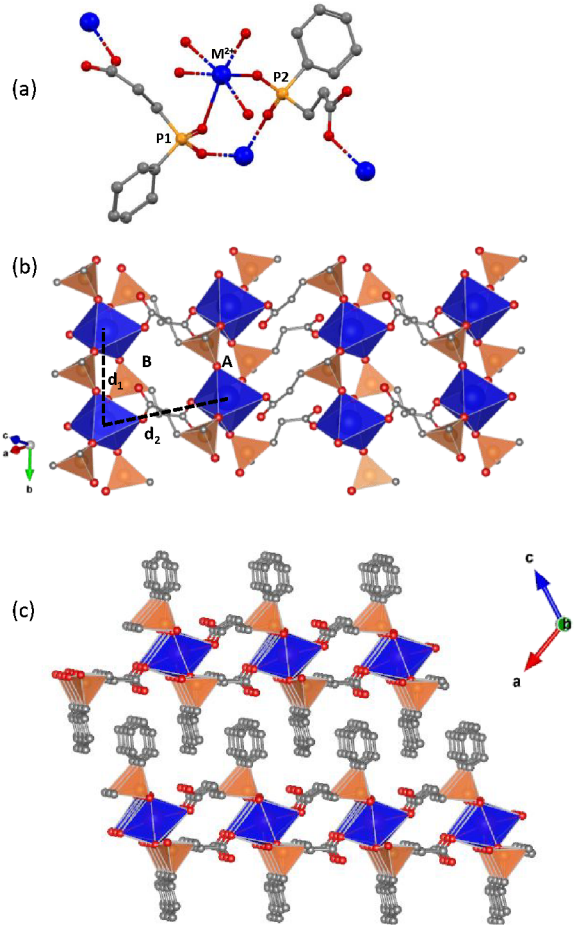

Figure 1. (a) Coordination environment and metal-ligand connectivity for compounds **1** and **2**; (b) detail of a layer of **2** showing the two types of rings A and B and the two distances between adjacent polyhedra; and (c) view of the packing of the layers in **2**. O_3PC tetrahedra, orange; CaO_6, blue; P, orange; O, red; C, grey.

The phenyl rings point toward the interlayer space and they arrange, between adjacent layers, in an interdigitated fashion and rotated slightly to each other, with short C···C distances, of 3.30 Å for 1 and 3.15 Å for **2** (Figure 1 and S5).

Structure of $Co_2[(O_2P(CH_2CH_2COO)(C_6H_5)(H_2O)]_2 \cdot 2H_2O$ (3)

This compound crystallizes in the *P2₁/a* (N° 14) space group (see Table 1), and contains 35 non-hydrogen atoms in the asymmetric unit: three crystallographically independent Co^{2+} ions, two of them (Co1 and Co2) in special position, two (Ph-PO_2-C_2H_4-$COO)^-$ ligands, and four water molecules (Figure 2). In contrast with the layered derivative previously reported,[5] that we have obtained by an alternative microwave assisted method (compound **4**), solid **3** displays a monodimensional structure consisting of CoO_6 polyhedra chains, with the phenyl groups pointing outside, as shown in Figure 2. The zig-zag chains are built up of edge-sharing Co^{2+} octahedra extended along the *c* axis direction. More precisely, these chains can be described as Co3-Co2-Co3 trimeric units linked through Co1. The coordination environment of Co1 and Co2 atoms are made-up exclusively by oxygens from the phosphinate ligand, whereas for Co3 atom, four oxygen atoms from four different ligands and two water oxygens (Ow1 and Ow2) form the octahedral environment. Each (Ph-PO_2-C_2H_4-$COO)^-$ anion acts as a bidentate ligand for Co1, through an oxygen atom from the phosphinate group (O11) and an oxygen atom (O41), most probably the non-protonated one, from the carboxylic group. In addition, O11 and O41 bridge Co1 and Co3 given rise to a shared edge between both cobalt atoms (Figure 2). Furthermore, the oxygen O21 from the phosphinate group binds monodentately to Co2. This metal-ligand connectivity is quite similar to that of Co(II) phenyl(carboxymethyl)phosphinate monohydrate, $[Co_2(PhPO_2\text{-}CH_2CO_2)_2(H_2O)_2]$ H_2O,[29] indicating that the connectivity can be preserved by hosting more lattice water molecules upon increasing the length of ligand alkyl chain.

The phosphonate groups are situated alternatively up and down of the Co atoms plane, with the phenyl groups in between the chains being rotated to each other, preventing thus establishing π···π interactions between aromatic rings of the same chain (Figure 2).

Each chain is surrounded by other six ones, with weak Van de Waals interactions between the phenyl groups. This arrangement forms isolated hydrophilic regions separated by hydrophobic environments of phenyl groups. H-bond interactions take place along a single chain between lattice water, coordinated water and unbound oxygen atom from the carboxylate group. In addition, interchain H-bonds are established through the lattice water (Table S2, Figure 2).

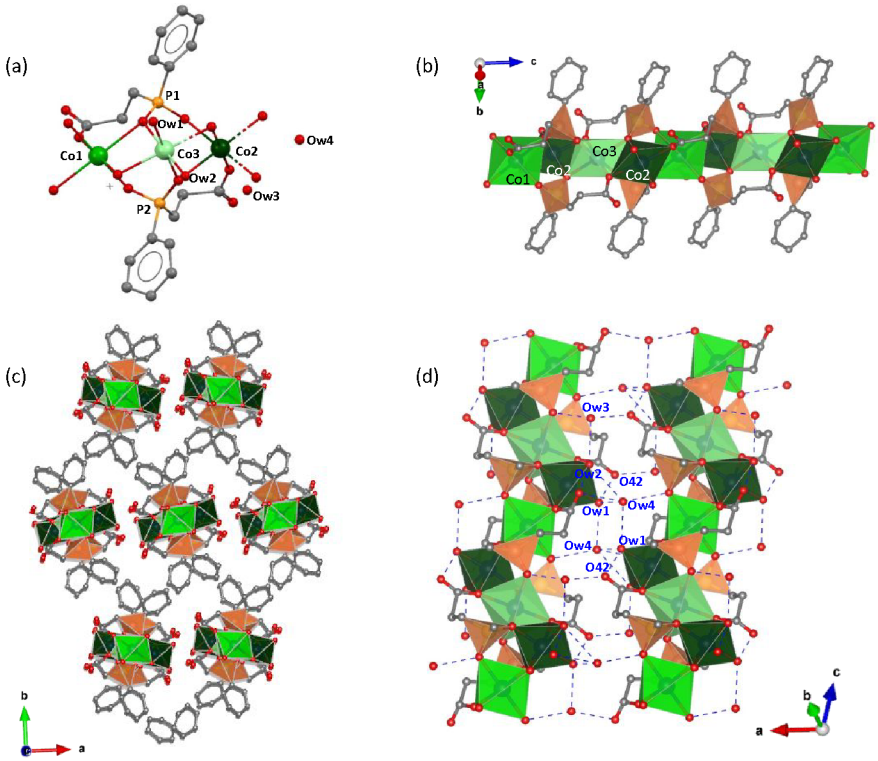

Figure 2. (a) Coordination environments for Co^{2+} atoms and metal-ligand connectivity for **3**; (b) 1D arrangement of the chains running along the c-axis; (c) packing of the 1-D chains; (d) H-bond network in the hydrophilic region. O_3PC tetrahedra, orange; CoO_6 octahedra, green.

Electrochemical characterization

The cobalt phosphinates (compounds **3** and **4**) were selected to evaluate their electrochemical properties, as cobalt electrocatalysts have been shown promising in OER and ORR processes.[30-32] We first carried out proton conductivity measurements to ascertain how efficient the existence of H-

bond in a cobalt phosphinate structure may be in establishing proton conduction pathways. The corresponding Nyquist plots for the parent phosphinic acid and compound **3**, at different temperatures and 95%RH are shown in Figure S5 and the Arrhenius plots are given in Figure S6. As can be seen, the formation of cobalt coordination polymers lowers the proton conductivity with respect to the phosphinic acid ($\sigma \sim 7{\cdot}10^{-5}$ $S{\cdot}cm^{-1}$ at 70 °C and 95% RH) dropping up to $2{\cdot}10^{-6}$ $S{\cdot}cm^{-1}$ for the cobalt derivative. Post-impedance analyses (TG curves and powder X-ray diffractions, Figures S7 and S8, respectively), revealed no changes under measurement conditions. The E_a values, lower than 0.4 eV, indicated a Grotthuss-type mechanism.[33] The low proton conductivity of cobalt phosphinate is attributed to isolation of the hydrophilic regions by phenyl groups that impede creating favorable extended proton conduction pathways.

To evaluate the eletrocatalytic properties, solids **3** and **4**, we have conducted different thermal treatments and analyzed the corresponding thermal decomposition products by PXRD and XPS. In comparison with compounds **1** and **2**, which exhibit weight losses in the TG curves, associated to decarboxylation and combustion of the organic moiety (Figure 3) before formation of the corresponding metal pyrophosphates, at 900 °C in air; cobalt compounds are characterized not only by the loss of water in two different stages (compound **3**), but also because the final decomposition products, at 900 °C, are compositionally distinct. Compound **3**, both in air and N_2 (Figure 3), shows two initial consecutive weight losses between RT and 200 °C. The first one due to the removal of one of the lattice water at 100 °C (calculated weight loss 2.93%, observed 2.74%) and a second corresponding to the elimination of the second lattice water together with the coordinated water molecules. The total weight loss observed at 200 °C, 11.20%, agrees well with the calculated, 11.72%. The resulting poorly crystalline anhydrous phase is stable up to 300 °C and fully recovers lattice water and crystallinity by exposure of the sample at 95% RH for 3 days (Figure S8). Complete thermal decomposition of **3** in air leads to the formation of the monoclinic $Co_2P_2O_7$ (PDF 01-084-2126, **3@900_O₂**) at 900 °C (Figure S9), whereas solid **4** decomposed, at the same temperature, in $Co_3(PO_4)_2$ (PDF 00-013-0503, **4@900_O₂**) (Table 2, Figure S10).

Under N_2, the thermal decomposition of **3** and **4** leads to different products. Thus, solid **3** decomposes between 360 and 600 °C giving $Co_2P_2O_7$ (**3@600_N₂**), which transforms, between 740 and 900 °C, to Co_2P (PDF 01-089-3030, (**3@1000_N₂**), as unique crystalline phase. Compound **4** experiences a transformation, between 400 and 600 °C, to an amorphous material, stable up to 700 °C, that further decomposes to Co_2P (PDF 01-089-3030, **4@1000_N₂**), at 1000 °C (Table 2, Figure S10).

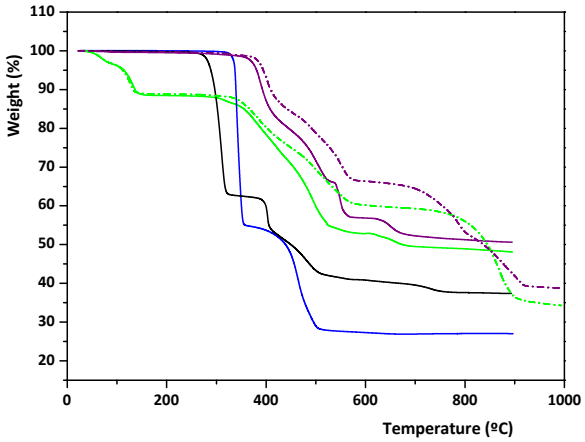

Figure 3. Thermogravimetric analyses in air (solid lines) and N_2 (dot lines) for **1** (black line), **2** (blue line), **3** (green line) and **4** (purple line).

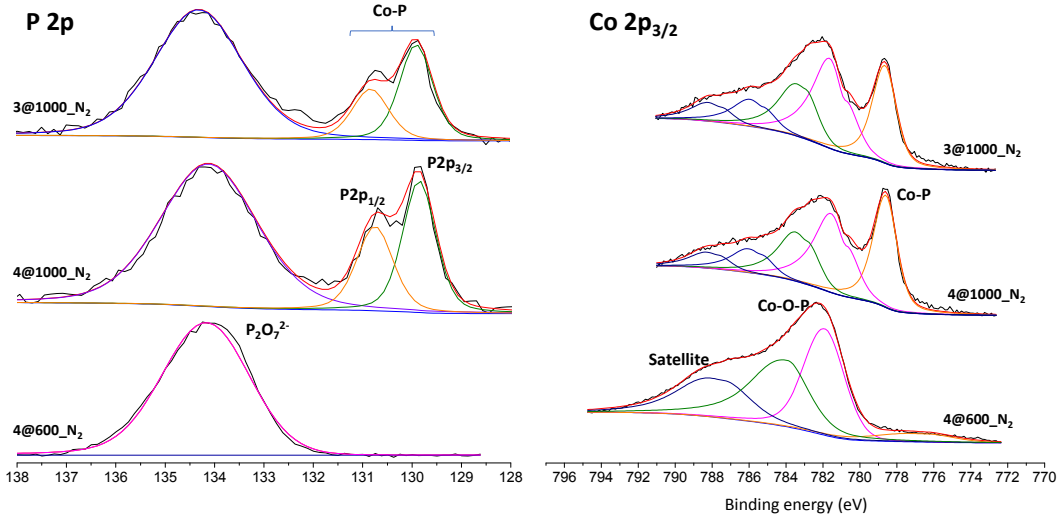

Figure 4. XPS of P 2p (left) and Co $2p_{3/2}$ (right) regions for pyrolyzed cobalt derivatives in N_2 at different temperatures.

XPS spectra in the Co ($2p_{3/2}$) region (Figure 4) displays two peaks depending on the pyrolytic treatment. The first one, observed as a unique peak in **4@600_N₂**, with a binding energy of ~781.92 eV, and associated satellite band, is characteristics of Co^{2+} ions in an oxygen environment in pyrophosphates.[34,35] The second one, present in samples **3** and **4** pyrolyzed at 1000 °C in N_2, is localized at 778.6 eV and can be attributed to Co^{2+} in a phosphide environment,[36] according to the PXRD identified

phase. In addition, the P 2p region shows a broad peak (134.2 eV), which is characteristic of P(V) in cobalt pyrophosphate[37] for **4@600_N_2**. However, for the 1000 °C-pyrolyzed samples, two other additional bands appear, at 130.7 eV and 129.8 eV, corresponding to phosphide ions bonded to Co^{2+}.[38,39]

The morphology of the samples was studied by scanning electron microscopy (SEM). Figure 5 shows SEM images for **3** and **4**, as well as for the corresponding pyrolyzed derivatives. For solid **3**, the as-prepared precursor presents a fibrous-like structure, with an average length of 5 μm, both, as single particles and bigger agglomerated particles. Such an agglomeration is more evident for the 200 °C-heated sample, treated in N_2. Upon pyrolysis at 600 °C, the sample adopts a more sheet-like morphology, while at 1000 °C globular particles are apparent. In the case of compound **4**, Figure 6, both precursor and 600 °C-pyrolyzed sample, exhibit a layered habit, although pyrolysis leads to size-decreased particles. At 1000 °C, compound **4**, calcined in N_2, is morphologically composed of small irregular (< 1 μm) particles that agglomerate in bigger aggregates.

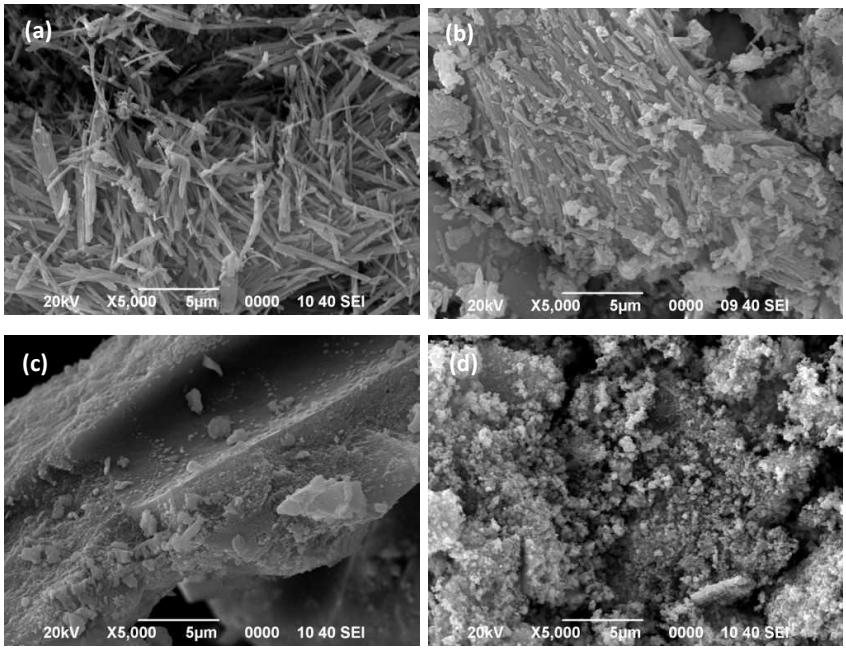

Figure 5. SEM images of 3 as: (a) as-synthesized, (b) 200 °C-heated, (c) pyrolyzed at 600 °C and (d) pyrolyzed at 1000 °C.

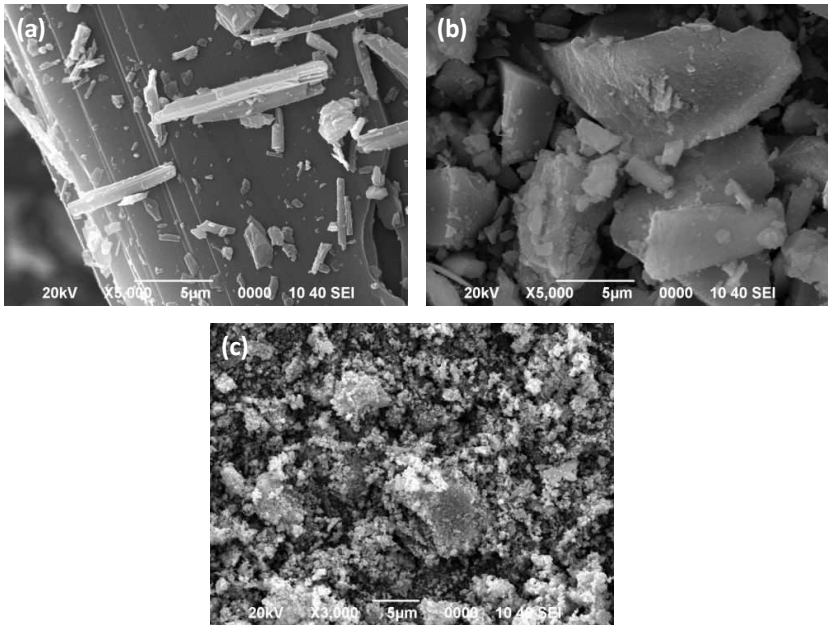

Figure 6. SEM micrographies of 4 as: (a) as-synthesized, (b) pyrolyzed at 600 °C and (c) pyrolyzed at 1000 °C.

In order to further explore the electrocatalytic properties of cobalt derivatives, against the oxygen evolution reaction, LSV curves and Tafel plots were determined. The overpotential values and the corresponding Tafel slopes are given in Table 2 and Figure 7.

Table 2. Phases, overpotential, Tafel slope and TOF values for compounds **3**, **4** and pyrolyzed derivatives.

Electrocatalyst	Phase	η_{10} (mV)	Tafel slope (mV·dec^{-1})	TOF (s^{-1}) (400 mV)
3	as-synthesized	351	58.5	0.056
4	as-synthesized	351	60.3	0.064
3@900_O$_2$	$Co_2P_2O_7$	371	107.4	0.011
4@900_O$_2$	$Co_3(PO_4)_2$	372	108.7	0.010
3@200_N$_2$	3-anhydrous	339	51.7	0.076
4@200_N$_2$	4	348	58.3	0.068
3@600_N$_2$	$Co_2P_2O_7$	382	60.8	0.028
3@1000_N$_2$	Co_2P	369	58.3	0.028
4@1000_N$_2$	Co_2P	372	53.5	0.035

The best OER performance in alkaline solution, is shown by 3@200_N_2 (phase 3-anhydrous). This electrocatalyst requires an overpotential of 339 mV, at a current density of 10 mA·cm^{-2}, and a lower Tafel slope, 51.7 mV·dec^{-1}, which reveals a more favorable reaction kinetic toward the OER than that of the as-synthesized compound. Although 3@200_N_2 may be similarly hydrated as the corresponding as-synthesized material, it apparently exhibits higher accessibility of the metal sites presumably by a combined effect of dehydration/rehydration and the surface loss of the ligand upon reaction (see below, Table S3). On the other hand, 4@200_N_2 does not exhibit improved electrocatalytic properties in comparison to the as-synthesized precursor (4), probably because the latter compound remains essentially the same upon heating at 200 °C (Figure 3). For the remaining solids, both as-synthetized and pyrolyzed derivatives, show slightly higher overpotential values, around 351 mV for the precursors, and close to 370 mV for $Co_2P_2O_7$ and/or Co_2P phases. In addition, the Tafel slopes also experiences a slight increase, excepting for 900 °C-calcined samples in air, which displayed the highest values, around 107-108 mV·dec^{-1}. For the latter compounds, the very low site accessibility might be associated to a high degree of particle agglomeration, as observed by SEM. Interestingly, the overpotential and Tafel slope determined for 3@200_N_2 compares well with those values found for another morphologically different $Co_2P_2O_7$ compound (359 mV and 54.1 mV·dec^{-1}),[40] metal phosphonates[18] or Co^{2+} pyrophosphates supported on different carbonaceous materials.[34, 41-43] Calculated TOF values (Table 2), in the range 0.010 – 0.076 s^{-1}, are of the order of those reported for other Co(II)-MOFs.[28, 44-45.] Figure S11 displays the Nyquist plots from the EIS measurements for the studied materials. It shows well-defined semicircles for all solids. **3@200C_N$_2$** displays the smallest semicircular diameter (R_c = 14.4 Ω), revealing the best OER performance for this material.

Preliminary studies to evaluate the electrocatalytic activity toward the ORR were carried out. The results indicate that theses solids shown a low catalytic capability (Figure S12) toward oxygen reduction. The onset potentials (E_{onset}) and halfwave potential ($E_{1/2}$) obtained from the LSV curves are far from those obtained for Pt/C benchmark (1.01 V and 0.90 V, respectively), being **3@1000_N$_2$** the solid with the best behavior (0.79 V and 0.66 V, respectively).

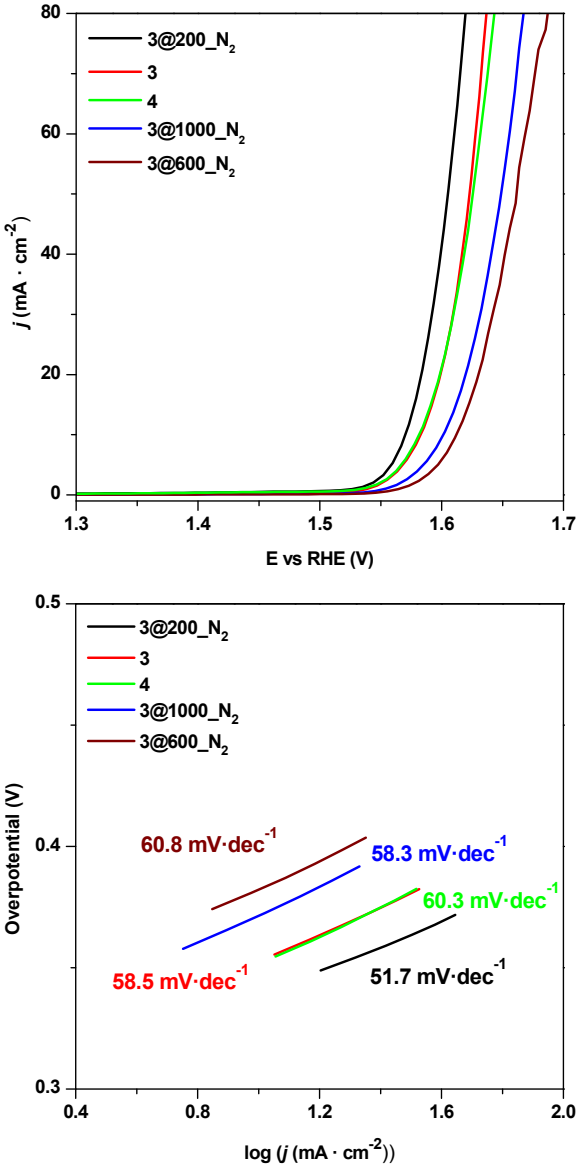

Figure 7. (a) LSV curves and (b) Tafel slopes for solids **3**, **4** and their pyrolytic products.

XPS analysis (Table S3), before and after OER and ORR tests, indicate that thermal treatments below 600 °C entail the surface loss of phosphorus (Table S3) due to hydrolysis in

alkaline solution.[41,46,47] On the other hand, the PXRD data (Figure S13) for solids calcined at 1000 °C show that the loss of phosphide, as revealed by XPS (Figure S14), is only superficial, since Co_2P is still present as the only crystalline phase after conducting the electrocatalytic tests.

Conclusions

While the structures of Ca^{2+} and Cd^{2+} (2-carboxyethyl)(phenyl)phosphinates follow the usual patterns of crystallization of related compounds, i.e. a layered topology of isolated metal octahedra, with interdigitated phenyl groups pointing to the interlayer space, the Co^{2+} derivative presents a characteristic 1D topology, of edge-sharing metal octahedra in zig-zag arrangement. Although H-bond interactions are established with the participation of water molecules and the ligand hydrophilic groups, the solid presents low proton conductivity attributed to the lack of extended H-bond networks, by the presence of bulky hydrophobic phenyl rings. Pyrolysis in air of as-synthesized Co^{2+} precursors lead to pyrophosphates/phosphates, whereas in N_2, crystalline Co_2P form at 1000 °C. Preliminary results indicate that, for OER, the pyrolyzed cobalt derivatives present a moderate activity comparable to other related material, but it could not be attributed to any specific Co^{2+} chemical environment.

Author Contributions

The manuscript was written through contributions of all authors. All authors have given approval to the final version of the manuscript.

Conflicts of interest

There are no conflicts to declare.

Acknowledgements

The work at UMA was supported by MICINN (Spain) through the research grants MAT2016-77648-R and PID2019-110249RB-I00 and FQM-113 research project (Junta de Andalucía, Spain). RMPC thanks UMA Research Plan for financial support. Selected XRD experiments were performed at BM04 beam-line at ALBA Synchrotron (proposal nº 2016091873) with the collaboration of ALBA staff.

References

1 S. J. Shearan, N. Stock, F. Emmerling, J. Demel, P.A. Wright, K.D. Demadis, M. Vassaki, F. Constantino, R. Vivani, S. Sallard, I.R. Salcedo, A. Cabeza and M. Taddei, *Crystals*, 2019, **9**, 270.
2 A. Clearfield, K.D. Demadis, Metal Phosphonate Chemistry: From Synthesis to Applications, A. Clearfield, K.D. Demadis, Eds.; Royal Society of Chemistry, **2012**.
3 A. Lenco, G. Tuci, A. Guerri and F. Costantino, *Crystals,* 2019, **9**, 283.
4 J. Rohlíček, D. Bužek, P. Brázda, L. Kobera, J. Hynek, J. Brus, K. Lang and J. Demel, *Crystals,* 2019, **9**, 303.
5 Z.-Y. Du, L. Zhang, B.-Y. Wang, S.-J. Liu, B. Huang, C.-M. Liu and W.-X. Zhang, *CrystEngComm.,* 2017, **19**, 1052.
6 W. Yang, H. Wang, W.-G. Tian, J. Li and Z.-M. Sun, *Eur. J. Inorg. Chem.*, 2014, **31**, 5378.
7 J. Li, C.-C. Xue, S. Liu and Z.-X. Wang, *Solid State Sci*., 2016, **61**, 111.
8 C. Atzori, K.A. Lomachenko, S. Øien-Ødegaard, C. Lamberti, N. Stock, C. Barolo and F. Bonino, *Cryst. Growth Des.,* 2019, **19**, 787.
9 R. Vincent and P.A. Midgley, *Ultramicroscopy,* 1994, **53**, 271.
10 W. Yang, D. Wu, C. Liu, Q.-J. Pan and Z.-M. Sun, *Crystal Growth Des*., 2016, **16**, 2011.
11 J. Hynek, P. Brázda, J. Rohlíček, M. G. S. Londesborough and J. Demel, *Angew. Chem. Int. Ed.,* 2018, **57**, 5016.
12 S. Midollini, P. Lorenzo-Luis and A. Orlandini, *Inorg. Chim. Acta,* 2006, **359***,* 3275.
13 A. Ienco, S. Midollini, A. Orlandini and F. Costantino, *Z. Naturforsch.,* 2007, **62b***,* 1476.
14 F. Costantino, A. Ienco, S. Midollini, A. Orlandini, L. Sorace and A. Vacca, *Eur. J. Inorg. Chem.,* 2008, **19**, 3046.
15 T. Bataille, S. Bracco, A. Comotti, F. Costantino, A. Guerri, A. Ienco and F. Marmottini, *CrystEngComm*., 2012, **14,** 7170.
16 H.-F. Wang, L. Chen, H. Pang, S. Kaskel and Q. Xu, *Chem.Soc.Rev.,* 2020, **49**, 1414.
17 Q. Liang, J. Chen, F. Wang and Y. Li, *Coord. Chem. Rev.,* 2020*,* **424**, 213488.
18 R. Zhang, P. A. Russo, A. G. Buzanich, T. Jeon and N. Pinna, *Adv. Funct. Mater*.,2017, **27**, 1703158.
19 Y. P. Zhu, C. X. Guo, Y. Zheng, S. Z. Qiao, *Acc. Chem. Res*., 2017, **50**, 915.
20 C. Tang and Q. Zhang, *J. Mater. Chem. A,* 2016, **4**, 4998.
21 R. Wang, X.-Y. Dong, J. Du, J.-Y. Zhao and S.-Q. Zang, *Adv. Mater*., 2018, **30**, 1703711.
22 G. H. Birum and R. F. Jansen*,* U.S. Patent, 4081463*,* 1978, Int. Cl.: C07F 9/30.
23 A. Altomare, C. Cuocci, C. Giacovazzo, A. Moliterni, R. Rizzi, N. Corriero and A. Falcicchio, *J. Appl. Cryst.,* 2013, **46**, 1231.
24 C. C. Xue, M. X. Li, M. Shao and Z. X. Wanga, *Russ. J. Coord. Chem.,* 2016, **42**, 442.
25 H. M. Rietveld, *J. Appl. Cryst.*, 1969, **2**, 65.
26 A. C. Larson and R. B. Von Dreele, Los Alamos National Laboratory Report LAUR 86-748, 2004.
27 B. H. J. Toby, *J. Appl. Cryst.,* 2001, **34**, 210.
28 S. Gutiérrez-Tarriño, J. L. Olloqui-Sariego, J. J. Calvente, G.o Mínguez Espallargas, F. Rey, A. Corma and P. Oña-Burgos, *J. Am. Chem. Soc.*, 2020, **142**, 19198.
29 S. Midollini, A. Orlandini, P. Rosa and L. Sorace, *Inorg. Chem*., 2005, **44**, 2060.
30 H. Zhao, C.-C. Weng, J.-T. Ren, L Ge, Y.-P. Liu and Z.-Y. Yuan, *Chin. J. Catal*., 2020*,* **41**, 259.
31 J.-T. Ren, G.-G. Yuan, L. Chen, C.-C. Weng and Z.-Y. Yuan, *ACS Sustainable Chem. Eng.,* 2018, **6**, 9793.
32 S. M. El-Refaei, P. A. Russo, P. Amsalem, N. Koch and N. Pinna, *ACS Appl. Nano Mater.,* 2020, **3**, 4147.
33 N. Agmon, *Chem. Phys. Lett.,* 1995, **244**, 456.
34 J.T. Ren, G.G. Yuan, L. Chen, C.-C. Weng and Z.-Y. Yuan, *ACS Sustainable Chem. Eng.,* 2018, **6**, 9793.
35 J. Feng, X. Cheng, J. T. Li and X. T. Luo, *ChemistrySelect,* 2018, **3**, 760.
36 J. Wu, D. Wang, S. Wan, H. Liu, C. Wang and X. Wang, *Small,* 2019, **16**, 1900550.
37 L. Ji, H. Zheng, Y. Wei, Y. Fang, J. Du, T. Wanga and S. Wang, *Sustainable Energy Fuels,* 2020, **4**, 1616.
38 T. Zhou, Y. Du, D. Wang, S. Yin, W. Tu, Z. Chen, A. Borgna and R. Xu, *ACS Catal.,* 2017, **7**, 6000.
39 X. Zhao, Y. Fan, H. Wang, C. Gao, Z. Liu, B. Li, Z. Peng, J.-H. Yang and B. Liu, *ACS Omega,* 2020, **5**, 6516.

40 H. Du, W. Ai, Z. L. Zhao, Y. Chen, X. Xu, C. Zou, L. Wu, L. Su, K. Nan, T. Yu and C. M. Li, *Small*, 2018, **14**, 1801068.
41 P. Bhanja, Y. Kim, K. Kani, B. Paul, T. Debnath, J. Lin, A. Bhaumik and Y. Yamauchi, *Chem. Eng. J.,* 2020, **396**, 1252452.
42 M. Pramanik, C. L. Li, M. Imura, V. Malgras, Y. M. Kang and Y. Yamauchi, *Small,* 2016, **12**, 1709.
43 C.-Z. Yuan, Y.-F. Jiang, Z. Wang, X. Xie, Z.-K. Yang, A. B. Yousaf and A.-W. Xu, *J. Mater. Chem. A,* 2016, **4**, 8155.
44 P. Liao, J. Q. Shen and J. P. Zhang, *Coord. Chem. Rev.,* 2018, **373**, 22.
45 X. Z. Song, N. Zhang, X. F. Wang and Z. Tan, *Mater. Today Energy*, 2021, **19**, 100597.
46 W. Xu, L. Feng, Z. Wang, B. Liu, X. Li and Y. Chen, *J. Electroanal. Chem.*, 2020, **879**, 114786.
47 M. Cao, S. Sun, C. Long, J. Luo and D. Wu, *Mater. Lett.*, 2021, **284**, 128891.